Passivity-Based Multisampled Converter-Side Current Control of *LCL*-Filtered VSCs

Shan He, *Member, IEEE*, Dao Zhou, *Senior Member, IEEE*, Xiongfei Wang, *Senior Member, IEEE*, and Frede Blaabjerg, *Fellow, IEEE*

***Abstract*—With the gradually decreasing cost of high-performance digital processors, multisampling current control is a potential method to reduce the control delay and improve the stability in *LCL*-filtered grid-connected converters. In the practical implementation, an antialiasing filter is required to remove the sampled switching harmonics and suppress the low-order aliasing. However, due to the phase lag from the antialiasing filter, the dissipative region of converter output admittance still cannot be lifted to switching frequency, which leads to a risk of system instability under wide grid admittance variation. In order to tackle this challenge, a filter capacitor voltage feedforward scheme using multisampling is proposed in this article. Consequently, the dissipation below the switching frequency is harvested for a three-phase converter. Furthermore, by doubling the multisampling rate, the proposed method can extend the dissipative region to the apparent switching frequency for a single-phase converter using unipolar modulation. The experimental results validate the effectiveness of the proposed method on a down-scaled single/three-phase converter.**

***Index Terms*—Current control loop, delay, dissipation, feedforward scheme, multisampling pulsewidth modulation (PWM), single/three-phase converter.**

I. Introduction

LCL-FILTERED grid-connected converters are widely used in distributed generation systems based on photovoltaic, wind turbine, and energy storage systems [1]. Nevertheless, with the large-scale penetration of renewable generation, the grid admittance seen from the point of common coupling varies in a wide range, which poses a significant challenge to the harmonic stability of the converter-grid system [2]. For example, even though the alternate-current controller (ACC) is designed with enough gain margin and phase margin (PM), the system may still be unstable when the phase difference is over 180° at the intersection point between the converter output admittance and the grid admittance [3], [4]. As an extension of the admittance shaping in the frequency domain, the passivity-based control is a promising solution to tackle the instability challenge. Specifically, only if the real part of the output admittance is nonnegative for all frequencies, the stable operation can be secured regardless of the grid admittance [5]. However, the pure passivity is impossible to obtain, and the upper boundary of the dissipative region is set to the Nyquist frequency [6].

Considering the control delay, the nondissipative region of the single-loop converter-side current control is located in the interval between the critical frequency (one-sixth of the sampling frequency) and the Nyquist frequency [7]. Filter capacitor current feedback-based active damping is an effective method to enhance the passivity, and the optimum damping coefficient is derived based on a general admittance model [8]. Actually, the filter capacitor current measurement is not always convenient and takes much cost, especially in the high-power applications [9]. If the filter capacitor current is estimated through a digital derivative, the phase-frequency characteristic around the switching frequency will not be accurate that weakens the damping performance [10]. An analog circuit-based high-pass filter is used to mimic the ideal derivative characteristic, but the cost and the implementation complexity are increased [7]. Another passivity enhancement route is to compensate for the control delay. Various terms are inserted in parallel with the ACC, such as high-pass filter [11], biquad filter [12], and a predictive term [13], but their compensation effect in the high-frequency range is limited. Besides, to suppress the inrush current during the startup and the grid faults, the grid voltage feedforward should be reserved, which is often ignored in the previous methods due to stability issues [14], [15].

Compared with single-sampling (SS) and double-sampling (DS) pulsewidth modulation (PWM), multisampling PWM is a potential candidate to reduce the nondissipative region since the control delay is inversely proportional to the sampling rate [16], [17]. Moreover, with the decreasing price of high-performance microprocessors, using multisampling PWM gradually becomes feasible in power electronic applications [18]. To suppress the low-order aliasing from the multisampled switching harmonics, an antialiasing filter is necessary but the extra phase lag is introduced [19]. Hence, the dissipation goal below the Nyquist frequency still cannot be met if only using single-loop control, and the extra active damping term is required. It is worth noting that the Nyquist frequency for the multisampling PWM is equal to the switching frequency instead of half sampling frequency,

Manuscript received 9 January 2022; revised 18 March 2022 and 17 May 2022; accepted 26 June 2022. Date of publication 1 July 2022; date of current version 26 July 2022. This work was supported in part by the Program of China Scholarships Council and in part by the Reliable Power Electronics-Based Power System Project at the Department of AAU Energy, Aalborg University, as a part of the Villum Investigator Program funded by the Villum Foundation. Recommended for publication by Associate Editor G. Oriti. *(Corresponding author: Frede Blaabjerg.)*

The authors are with the AAU Energy, Aalborg University, 9220 Aalborg, Denmark (e-mail: she@energy.aau.dk; zda@energy.aau.dk; xwa@energy.aau.dk; fbl@energy.aau.dk).

Color versions of one or more figures in this article are available at https://doi.org/10.1109/TPEL.2022.3187575.

Digital Object Identifier 10.1109/TPEL.2022.3187575

this is because multisampling PWM is equivalent to a DS PWM with the sampling instant shift and the update instant shift.

On the other hand, for a single-phase H-bridge (HB) converter with unipolar modulation, the four-sampling control is usually recommended since no switching harmonics are introduced [20], [21]. The apparent switching frequency is twice larger than the preset switching frequency, and the four-sampling control can be regarded as a DS control. Then, the dissipative region is the same as the regular sampling control, and the advantage of multisampling PWM on the control delay reduction is not fully exploited.

To lift the dissipative region for a multisampling-controlled three-phase converter, a filter capacitor voltage feedforward scheme is proposed in this article. Specifically, 8 samplings with proportional–derivative (PD) feedforward or 16 samplings with P feedforward can achieve the dissipation below the switching frequency, which is the first contribution of this article. Furthermore, the issues related to the cost and transients are solved at the same time. Then, the proposed method is extended to a single-phase converter by doubling the sampling rate based on the apparent switching frequency, and the dissipative region is lifted to the apparent switching frequency instead of the preset switching frequency. This is the second contribution of this article.

The rest of this article is organized as follows. Section II derives the dissipative region of ACC using regular sampling and multisampling. Then, a filter capacitor voltage feedforward scheme is presented in Section III. Next, the analysis of the single/three-phase converters with different feedforward terms and sampling rates are given. The experimental results for validating the effectiveness of the proposed method are presented in Section IV. Finally, Section V concludes this article.

II. Passivity Analysis of ACC

A. System Model

Fig. 1(a) shows a single-loop current control diagram for a three-phase converter, where U_{ga}, U_{gb}, and U_{gc} are the grid voltages, U_{ca}, U_{cb}, and U_{cc} are the filter capacitor voltages, $U_{\rm dc}$ is the dc-link voltage, i_{con} is the converter-side current, i_g is the grid-side current, L_1 is the converter-side inductance, L_2 is the grid-side inductance, and C is the filter capacitance, respectively. The single-loop current control of a single-phase converter is presented in Fig. 1(b), where U_g is the grid voltage and U_c is the filter capacitor voltage. Fig. 1(c) illustrates the model of the single-loop ACC in a static frame, which is applicable for the single/three-phase converters. i^*_{condq} and $i^*_{con\alpha\beta}$ are the current references in the dq- and $\alpha\beta$-frame, respectively. Regarding C and L_2 as the grid admittance, only the converter-side inductance needs to be considered and the plant model $G_p(s)$ is

$$G_p(s) = \frac{1}{sL_1}. \tag{1}$$

$G_d(s)$ is the control delay, including the computation delay and PWM delay, which is given as

$$G_d(s) = e^{-sT_d}. \tag{2}$$

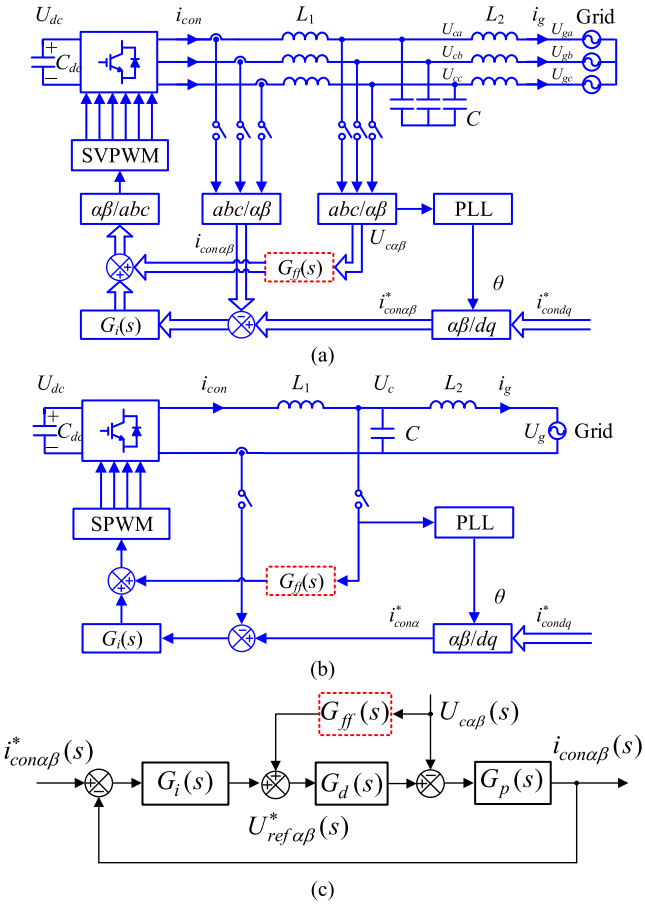

Fig. 1. Current control diagram of a single/three-phase grid-connected converter. (a) Three-phase control diagram. (b) Single-phase control diagram. (c) General current control model.

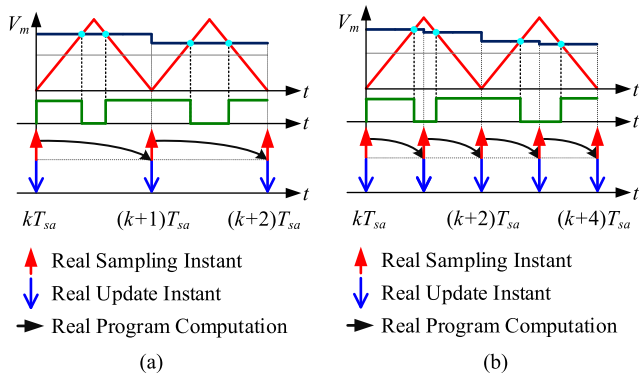

Fig. 2. Regular sampling PWM. (a) SS PWM. (b) DS PWM.

$G_i(s)$ is the proportional–resonant controller, which is

$$G_i(s) = K_p + K_r\omega_{rc}\frac{s\cos\varphi_g - \omega_g\sin\varphi_g}{s^2 + \omega_{rc}s + \omega_g^2} \tag{3}$$

where ω_g, ω_{rc}, φ_g, K_p, and K_r are the fundamental angle frequency, the cut-off angle frequency of the resonant controller, the compensation angle of the resonant controller, the proportional controller gain, and the resonant controller gain, respectively.

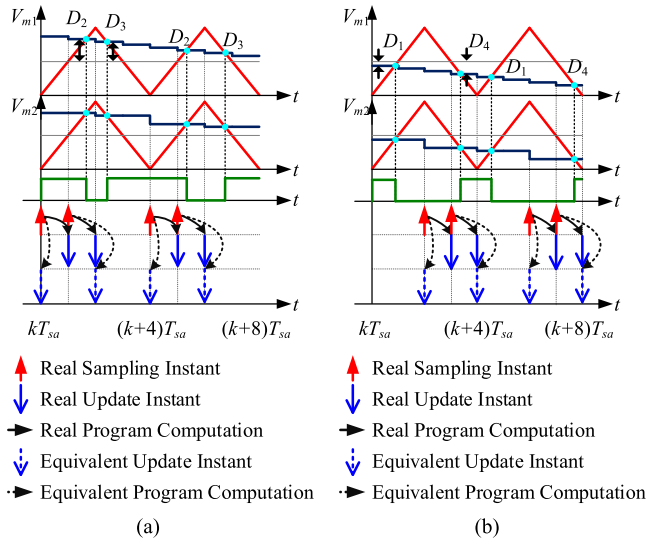

Fig. 3. General multisampling PWM. (a) Positive half cycle. (b) Negative half cycle.

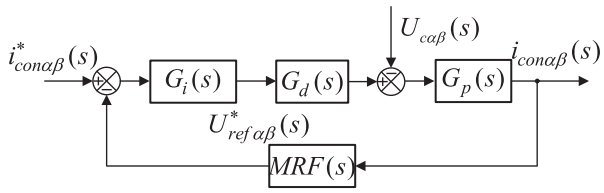

Fig. 4. Single-loop current control diagram using multisampling (MRF: modified repetitive filter).

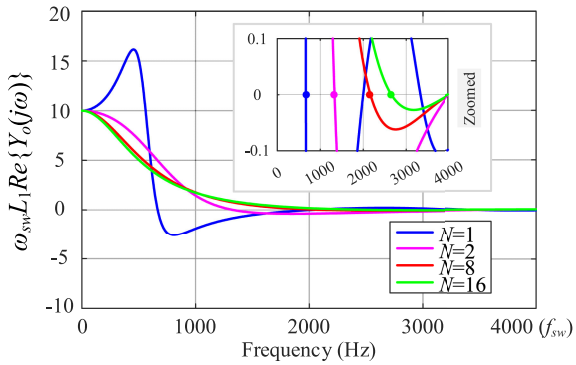

Fig. 5. Real part of output admittance for a single-loop converter-side current controller using regular sampling ($N = 1, 2$), 8 samplings ($N = 8$), and 16 samplings ($N = 16$) for three-phase converters.

Based on Fig. 1(c), the output converter-side current in the static frame is

$$i_{con}(s) = G_{cl}(s)i^*_{con}(s) - Y_o(s)U_c(s) \tag{4}$$

where $G_{cl}(s)$ is the closed-loop transfer function between the reference current and the feedback current, and $Y_o(s)$ is the output admittance with the ACC. Their expressions are as follows:

$$G_{cl}(s) = \frac{G_d(s)G_i(s)G_p(s)}{1 + G_d(s)G_i(s)G_p(s)} \tag{5}$$

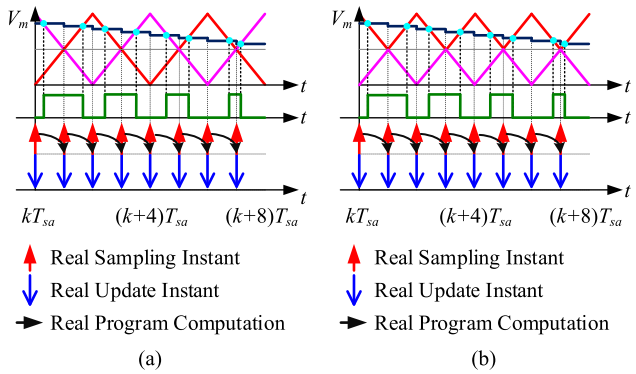

Fig. 6. Four-sampling PWM for a single-phase H-bridge converter. (a) Seen from a preset switching frequency perspective. (b) Seen from an apparent switching frequency perspective.

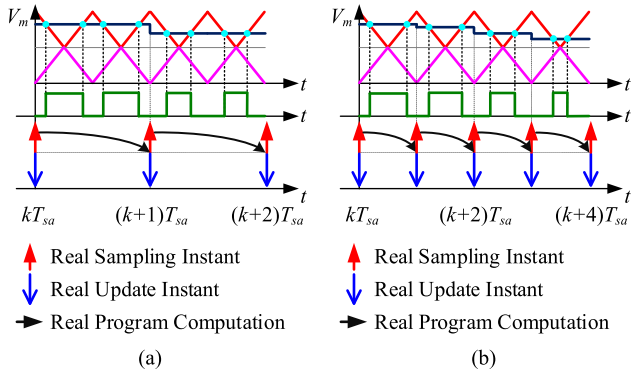

Fig. 7. Regular sampling PWM for a single-phase H-bridge converter. (a) SS seen from an apparent switching frequency perspective. (b) DS seen from an apparent switching frequency perspective.

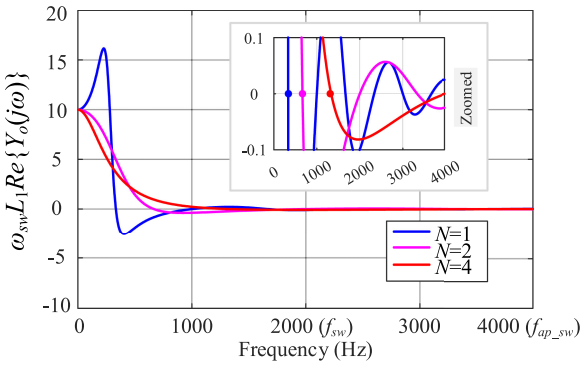

Fig. 8. Real part of output admittance for a single-loop converter-side current controller using regular sampling ($N = 1, 2$) and four samplings ($N = 4$) for a single-phase converter.

$$Y_o(s) = \frac{G_p(s)}{1 + G_d(s)G_i(s)G_p(s)}. \tag{6}$$

According to the passivity-based theory, a grid-connected converter can be stabilized if the following two constraints are satisfied. First, the closed-loop transfer function in (5) should be

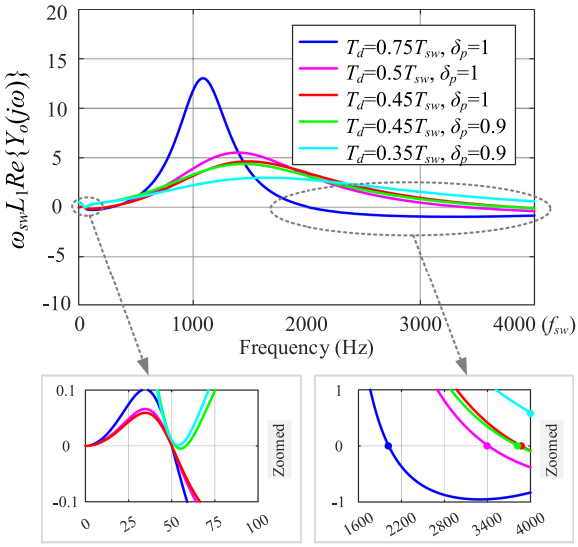

Fig. 9. Real part of output admittance with proportional feedforward and different control delays.

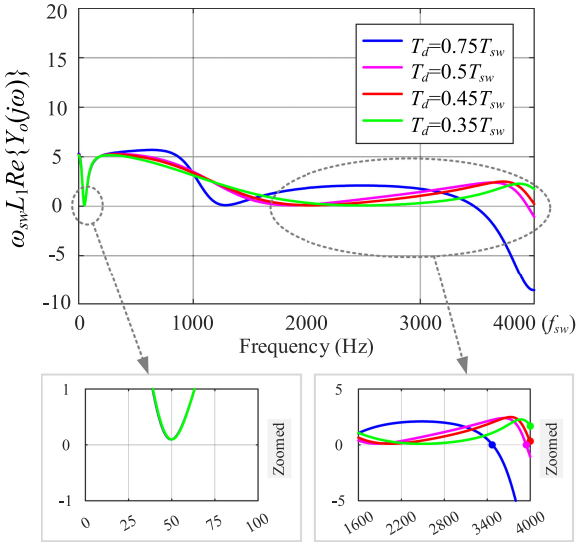

Fig. 10. Real part of output admittance with derivative feedforward and different control delays.

stable. For a given PM, the maximum bandwidth r_b is

$$r_b = \frac{\omega_c}{\omega_{sw}} = \frac{0.5\pi - \varphi_m}{T_d\omega_{sw}} = \frac{0.5\pi - \varphi_m}{2\pi h}. \tag{7}$$

The control delay T_d is expressed as $T_d = hT_{sw}$, where T_{sw} is the switching period. φ_m is the PM, ω_c is the crossover angle frequency, and ω_{sw} is the switching angle frequency. If φ_m is set to 0.25π and the bandwidth is set from 0.1 to 0.2, the allowed maximum control delay T_d should be in the interval of $[0.625T_{sw}, 1.25T_{sw}]$ [22].

For the regular SS and DS PWM, as shown in Fig. 2, the control delay (computation delay and PWM delay) is $1.5T_{sw}$ or $0.75T_{sw}$, respectively [23]. Hence, the maximum bandwidth using DS PWM can be one-sixth when the PM is 0.25π, which

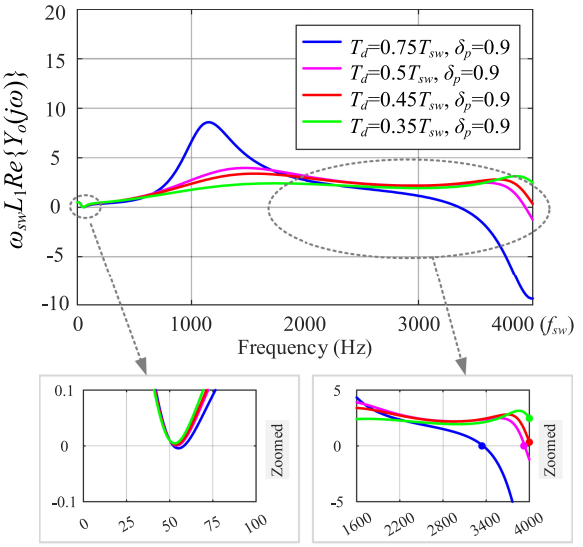

Fig. 11. Real part of output admittance with PD feedforward and different control delays.

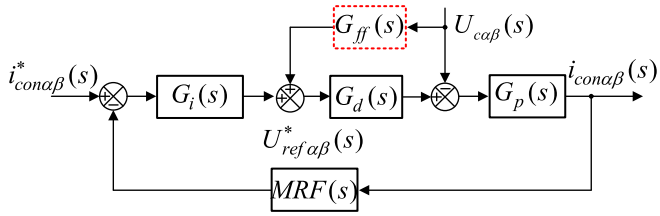

Fig. 12. Multisampled converter-side current control diagram with filter capacitor voltage feedforward (MRF: modified repetitive filter).

means that the inner stability in (8) can be easily secured. Second, the phase of $Y_o(s)$ should be within $[-90°, 90°]$ below Nyquist frequency. Since the control delay mainly affects the passivity in the high-frequency range, the R controller can be temporarily neglected. Then, $Y_o(s)$ in (6) is simplified as follows:

$$Y_o(s) \approx \frac{1}{sL_1 + K_p e^{-sT_d}}. \tag{8}$$

By substituting "$s = j\omega$" into (8), $\mathrm{Re}\{Y_o(j\omega)\}$ is given as follows:

$$\mathrm{Re}\{Y_o(j\omega)\} \approx \frac{K_p\cos(\omega T_d)}{(K_p\cos(\omega T_d))^2 + (\omega L_1 - K_p\sin(\omega T_d))^2}. \tag{9}$$

According to (9), the sign of $\mathrm{Re}\{Y_o(j\omega)\}$ is determined by the numerator, and the dissipative region is

$$f_{\text{dissipative}} = \left(0, \frac{1}{4T_d}\right). \tag{10}$$

Then, the dissipative region for SS and DS PWM is $(0, \frac{1}{6}f_{sw})$ and $(0, \frac{1}{3}f_{sw})$, respectively. It can be seen that only if the control delay T_d is smaller or equal to $0.25T_{sw}$, the dissipative region can be lifted to the switching frequency. Hence, the regular sampling PWM cannot satisfy the dissipation requirement if using single-loop converter-side current control.

B. Multisampled Current Control for Three-Phase Converters

Multisampling PWM is a potential candidate to reduce the control delay physically, and the control delay is inversely proportional to the sampling rate N [16], [17], which is given as follows:

$$T_{d\_MS} = \frac{1.5T_{sw}}{N}. \tag{11}$$

The general multisampling PWM is shown in Fig. 3, where the state variable is sampled and the duty cycle is updated multiple times within one switching period. Since only two duty cycles are effective within one switching period, based on the voltage-second balance, the multisampling PWM is equal to a DS PWM with the sampling instant shift and the update instant shift. That is to say, the Nyquist frequency for multisampling PWM is equal to the switching frequency [19]. Ideally, when the sampling rate is greater or equal to six, the dissipation goal can be met based on (10) and (11). However, to suppress the low-order aliasing caused by the sampled switching harmonics, a modified repetitive filter (MRF) should be inserted in the feedback path and an extra phase lag is introduced [24], [25], as shown in Fig. 4. The MRF contains a compromised moving average filter and a delay compensator, and the expression of MRF is

$$\begin{aligned}\mathrm{MRF}(s) &= \underbrace{\frac{2}{N}\frac{1-e^{-NsT_{sa}}}{1-e^{-2sT_{sa}}}}_{\mathrm{CMAF}} + \underbrace{\frac{1-r^N}{1-r^2}\frac{1-r^2e^{-2sT_{sa}}}{1-r^Ne^{-NsT_{sa}}}}_{\mathrm{Delaycompensator}} \\ &\approx e^{-0.25sT_{sw}}\end{aligned} \tag{12}$$

where $r \in (0, 1)$ is called the attenuation factor. There is a tradeoff between the delay compensation performance and high-frequency noise suppression ability in terms of the variation of r [24], [25]. Consequently, the total loop delay, including the control delay and the MRF delay, is

$$\begin{aligned}T_{d\_MS\_\mathrm{MRF}} &= \underbrace{\frac{1.5}{N}T_{sw}}_{\mathrm{Computationdelay+PWMdelay}} + \underbrace{0.25T_{sw}}_{\mathrm{MRFdelay}} \\ &= \frac{6+N}{4N}T_{sw}.\end{aligned} \tag{13}$$

Similarly, substituting (13) into (10), the dissipative region using multisampling PWM with MRF is given as

$$f_{\mathrm{dissipative\_}MS\_\mathrm{MRF}} = \left(0, \frac{N}{6+N}f_{sw}\right). \tag{14}$$

Based on the parameters of a three-phase grid-connected converter in Table I, the comparison of $\mathrm{Re}\{Y_o(j\omega)\}$ using different sampling rates is given in Fig. 5. The bandwidth is set to $0.1f_{sw}$ to make the closed-loop function stable for all the sampling cases, and the resonant controller is ignored for the analysis in the high-frequency range. It can be seen that the eight samplings can reduce the nondissipative region compared with SS and DS, but they still cannot achieve the dissipation below the switching frequency. With the increase of sampling rate N, such as 16 samplings, the nondissipative region can be further reduced. However, due to the limited computation ability of digital processors, the allowed maximum sampling frequency cannot be infinite. Therefore, multisampled single-loop control with converter-side current feedback cannot meet the dissipation goal, and extra damping is required.

TABLE I
MAIN PARAMETERS OF A THREE-PHASE GRID-CONNECTED CONVERTER

Symbol	Description	Value	Symbol	Description	Value
P_o	Output power	7 kW	U_{grms}	Grid voltage (Phase-to-ground RMS voltage)	220 V
U_{dc}	DC-link voltage	700 V	C_{dc}	DC-link capacitance	297 μF
L_1	Converter-side inductance	4 mH	L_2	Grid-side inductance	2 mH
C	Filter capacitance	3 μF	f_{sw}	Switching frequency	4 kHz
f_r	Resonance frequency	2516 Hz	f_{sa8}	Sampling frequency	32 kHz
f_{sa16}	Sampling frequency	64 kHz	r_8	Attenuation factor	0.6
r_{16}	Attenuation factor	0.8	δ_{p8}	Proportional feedforward coefficient	0.9
δ_{d8}	Derivative feedforward coefficient	2.4e-5 s	δ_{p16}	Proportional feedforward coefficient	0.9
K_p	Proportional controller gain	20 Ω	K_r	Resonant controller gain	1000 Ω/s

C. Multisampled Current Control for Single-Phase Converters

For a single-phase H-bridge converter with unipolar modulation, the apparent switching frequency is twice larger than the preset switching frequency. As shown in Fig. 6(a), the sampling rate is usually set to four, and the sampling instants are located at the peak/valley points and the intersection points of the interleaved carriers [20], [21]. If considering the apparent switching frequency as the base value, four-sampling control can be regarded as a DS control [see Fig. 6(b)], which is the reason why no switching harmonics are introduced in the four-sampled current. Moreover, the Nyquist frequency is equal to the apparent switching frequency f_{ap_sw} when using four-sampling control. Hence, the control delay and the dissipative region should be reevaluated. The four-sampling control delay is equal to $0.75T_{eq\_sw}$, which is given as

$$\begin{aligned}T_{d\_4S} &= \underbrace{\frac{T_{sw}}{4}}_{\mathrm{ComputationDelay}} + \underbrace{\frac{T_{sw}}{8}}_{\mathrm{PWMDelay}} = \frac{1.5T_{sw}}{4} \\ &= \underbrace{\frac{T_{ap\_sw}}{2}}_{\mathrm{ComputationDelay}} + \underbrace{\frac{T_{ap\_sw}}{4}}_{\mathrm{PWMDelay}} = \frac{1.5T_{ap\_sw}}{2}.\end{aligned} \tag{15}$$

Substituting (15) into (10), the dissipative region using four-sampling PWM is given as

$$f_{\mathrm{dissipative\_}4S} = \left(0, \frac{1}{3}f_{ap\_sw}\right). \tag{16}$$

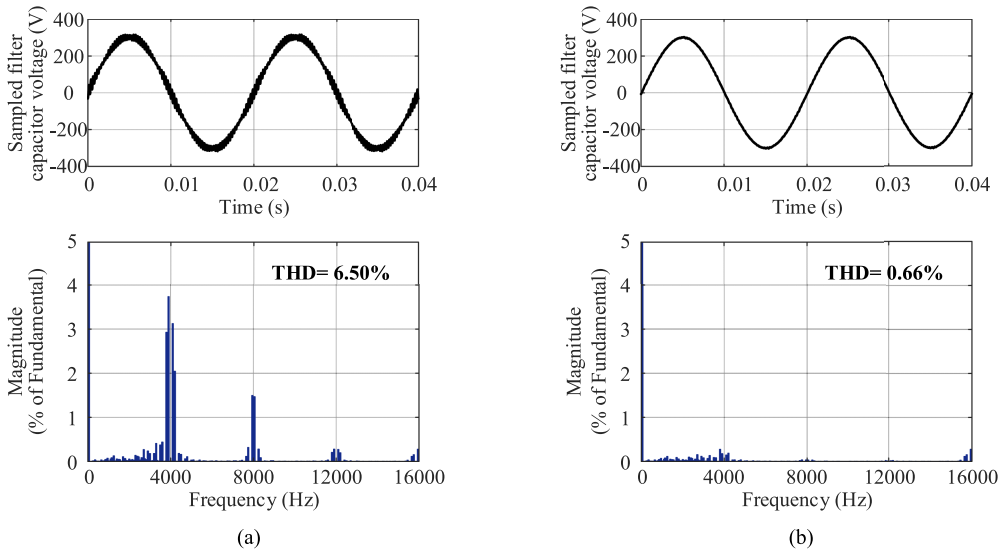

Fig. 13. Eight-sampled filter capacitor voltage in a three-phase system and its harmonic spectrum. (a) Without MRF. (b) With MRF.

TABLE II
MAIN PARAMETERS OF A SINGLE-PHASE GRID-CONNECTED CONVERTER

Symbol	Description	Value	Symbol	Description	Value
P_o	Output power	2.3 kW	U_{grms}	Grid voltage (Phase-to-ground RMS voltage)	220 V
U_{dc}	DC-link voltage	360 V	C_{dc}	DC-link capacitance	198 μF
L_1	Converter-side inductance	4 mH	L_2	Grid-side inductance	2 mH
C	Filter capacitance	3 μF	f_{sw}	Switching frequency	2 kHz
f_r	Resonance frequency	2516 Hz	f_{sa16}	Sampling frequency	32 kHz
f_{sa32}	Sampling frequency	64 kHz	r_{16}	Attenuation factor	0.6
r_{32}	Attenuation factor	0.8	δ_{p16}	Proportional feedforward coefficient	0.9
δ_{d16}	Derivative feedforward coefficient	2.4e-5 s	δ_{p32}	Proportional feedforward coefficient	0.9
K_p	Proportional controller gain	20 Ω	K_r	Resonant controller gain	1000 Ω/s

Similarly, it can be seen from Fig. 7 that the conventional DS control is equivalent to an SS control, and the conventional SS control is equivalent to an SS control with an extra one-step delay. Then, the dissipative region for SS and DS PWM is $(0, \frac{1}{12}f_{ap\_sw})$ and $(0, \frac{1}{6}f_{ap\_sw})$, respectively.

The parameters of a down-scaled single-phase grid-connected converter are given in Table II. The switching frequency is set to 2 kHz, and the apparent switching frequency is 4 kHz. Hence, the *LCL* filter parameters can be designed as same as the three-phase system. According to (16), the dissipative region using four samplings is still far away from the Nyquist frequency, as shown in Fig. 8. Again, only using four-sampled single-loop control

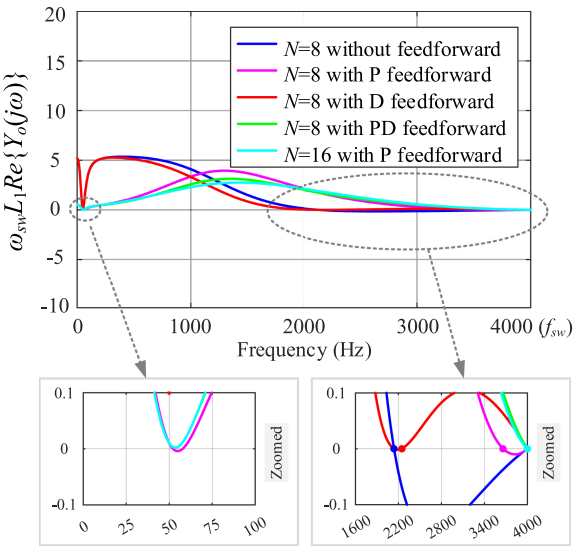

Fig. 14. Real part of output admittance with and without filter capacitor voltage feedforward based on different sampling rates for three-phase converters.

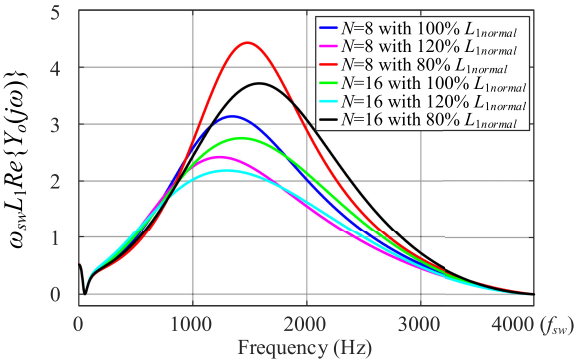

Fig. 15. Robustness analysis of the proposed method against converter-side inductance variation ($N = 8$ with PD feedforward or $N = 16$ with P feedforward).

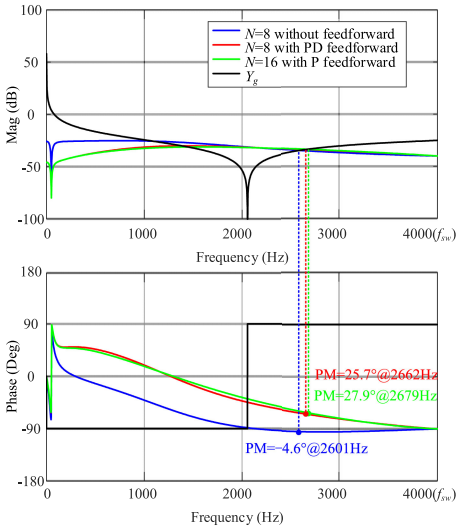

Fig. 16. Output admittance for a multisampled three-phase converter with and without the filter capacitor voltage feedforward.

cannot achieve the dissipation goal, and the extra damping term is required. It is worth noting that the sign of $\mathrm{Re}\{Y_o(j\omega)\}$ for the conventional SS and DS changes more than once, that is, because the Nyquist frequency is $0.5f_{sw}$ and f_{sw}, respectively [26].

On the other hand, it is reported that using single-phase cascaded H-bridge (CHB) converters can help to reduce the control delay [21], which is given as

$$T_{d\_\mathrm{CHB}} = \underbrace{\frac{T_{sw}}{4M}}_{\mathrm{ComputationDelay}} + \underbrace{\frac{T_{sw}}{8M}}_{\mathrm{PWMDelay}} = \frac{1.5T_{sw}}{4M} = \underbrace{\frac{T_{ap\_sw}}{2}}_{\mathrm{ComputationDelay}} + \underbrace{\frac{T_{ap\_sw}}{4}}_{\mathrm{PWMDelay}} = \frac{1.5T_{ap\_sw}}{2} \quad (17)$$

where M is the number of cascaded cells. The apparent switching frequency is $2Mf_{sw}$ and the multisampling rate is set to $4M$. Under this condition, the control delay can be further reduced compared with the single cell. If considering the apparent switching frequency as the base value, it is still a DS control and the dissipative region is

$$f_{\mathrm{dissipative\_CHB}} = \left(0, \frac{1}{3}f_{ap\_sw}\right). \quad (18)$$

Compared with (16), the passivity is not enhanced by increasing the number of cascaded cells, and the focus should go back to the passivity enhancement of a single cell.

III. Passivity Enhancement

A. General Analysis Using Proportional Feedforward and Derivative Feedforward With Different Control Delays

The filter capacitor voltage P feedforward and D feedforward are the most commonly used damping methods, and their effects on the passivity in terms of control delay are evaluated in this section. The feedforward function is given as

$$G_{ff}(s) = \delta_p + \delta_d s \quad (19)$$

where δ_p and δ_d are the P feedforward coefficient and D feedforward coefficient, respectively. Ignoring the R controller, the output admittance is

$$Y_o(s) \approx \frac{1 - e^{-sT_d}\delta_p - e^{-sT_d}\delta_d s}{sL_1 + K_p e^{-sT_d}}. \quad (20)$$

By substituting "$s = j\omega$" into (20), $\mathrm{Re}\{Y_o(j\omega)\}$ is given as

$$\mathrm{Re}\{Y_o(j\omega)\} \approx \frac{\overbrace{K_p\cos(\omega T_d)}^{\mathrm{Single-loopcontrol}} \overbrace{-\delta_p K_p + \delta_p \omega L_1 \sin(\omega T_d)}^{\mathrm{Proportionalfeedforward}}}{(K_p\cos(\omega T_d))^2 + (\omega L_1 - K_p\sin(\omega T_d))^2} - \frac{\overbrace{-\delta_d\omega^2 L_1\cos(\omega T_d)}^{\mathrm{Derivativefeedforward}}}{(K_p\cos(\omega T_d))^2 + (\omega L_1 - K_p\sin(\omega T_d))^2}. \quad (21)$$

If only considering the P feedforward, the sign of $\mathrm{Re}\{Y_o(j\omega)\}$ is determined by $\delta_p\omega L_1\sin(\omega T_d)$ instead of $K_p\cos(\omega T_d)$ [8], and the dissipative region is given as

$$f_{\mathrm{dissipative}} = \left(0, \frac{1}{2T_d}\right). \quad (22)$$

According to (22) and (10), the allowed maximum delay for dissipation increases twice, which can easily be met using multisampling. The real part of the output admittance considering P feedforward and different control delays is given in Fig. 9. The controller parameters in Table I are used in the analysis. It can be seen that when the control delay is equal to $0.5T_{sw}$, the sign of $\mathrm{Re}\{Y_o(j\omega)\}$ around the switching frequency is negative, which can be removed when the control delay is small enough, e.g., $0.35T_{sw}$. In addition, the P coefficient should be lower than one since the R controller will affect the stability in the low-frequency range.

On the other hand, if only using D feedforward, the dissipation below the switching frequency can be achieved by changing the sign of $\mathrm{Re}\{Y_o(j\omega)\}$ at the critical frequency [9]. The D coefficient is given as

$$\delta_d = \frac{4T_d^2 K_p}{\pi^2 L_1}. \quad (23)$$

Moreover, the ideal derivative does not exist in the practical implementation [17], and a digital derivative is given as

$$dev(s) = \frac{1.8}{T_{sa}}\frac{1 - e^{-sT_{sa}}}{1 + 0.8e^{-sT_{sa}}}. \quad (24)$$

where T_{sa} is equal to the DS period in this section. As shown in Fig. 10, the stability around the critical frequency is weak that can be easily affected by the R controller [27]. In addition, the nondissipative region around the switching frequency appears again and the control delay should be lower than $0.5T_{sw}$. If combining the P feedforward and D feedforward, the stability around the critical frequency can be enhanced. In addition, when the control delay is lower than $0.5T_{sw}$, the stability around the

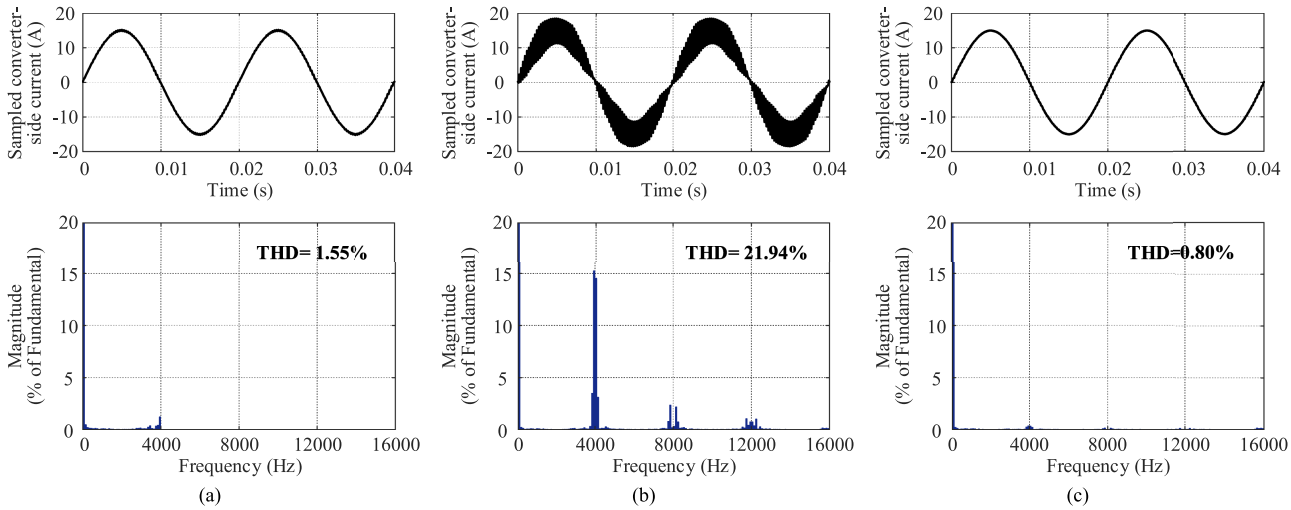

Fig. 17. Multisampled converter-side current in a single-phase HB converter and its harmonic spectrum. (a) 4-sampled converter-side current. (b) 16-sampled converter-side current without MRF. (b) 16-sampled converter-side current with MRF.

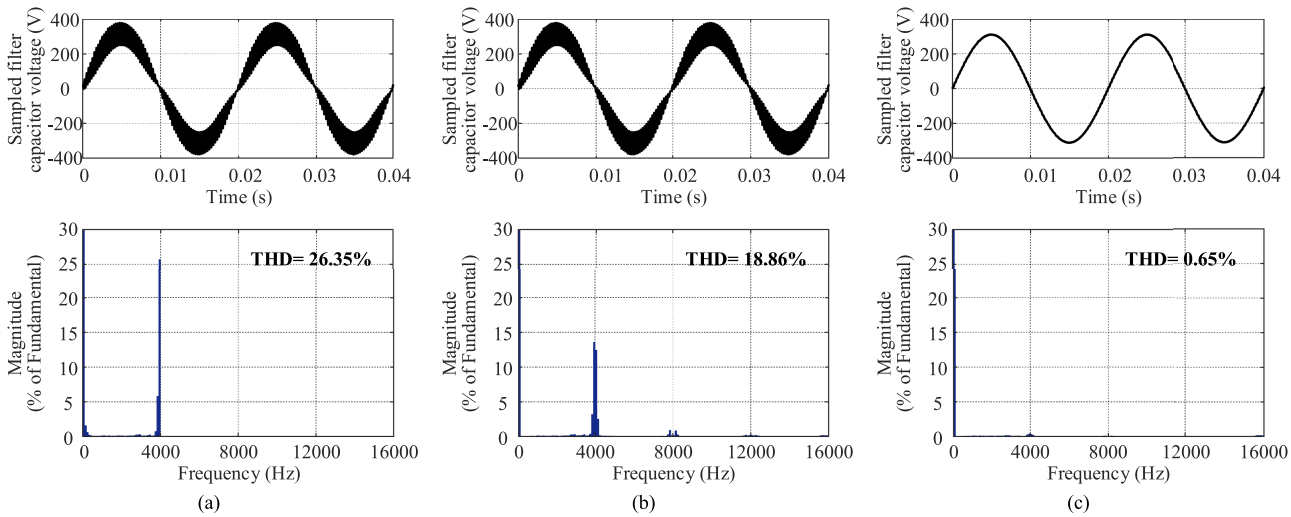

Fig. 18. Multisampled filter capacitor voltage in a single-phase HB converter and its harmonic spectrum. (a) 4-sampled filter capacitor voltage. (b) 16-sampled filter capacitor voltage without MRF. (b) 16-sampled filter capacitor voltage with MRF.

switching frequency can also be enhanced (see Figs. 9 and 11 when the delay is $0.45T_{sw}$).

To summarize, if the multisampled loop delay is small enough, the first choice is to use the P feedforward since the derivative may amplify the noise. At the same time, the proportional coefficient should be lower than one to secure the low-frequency dissipation. If the P feedforward cannot meet the goal, then add the D feedforward but the loop delay should be lower than $0.5T_{sw}$.

B. Multisampled Current Control of the Three-Phase Converters

Fig. 12 shows the multisampled current control diagram with the filter capacitor voltage feedforward. Especially, besides the MRF in the converter-side current feedback path, the MRF should also be inserted in the feedforward path to remove the sampled switching harmonics and suppress the aliasing. The feedforward function is given as

$$G_{ff}(s) = \delta_p \mathrm{MRF}(s) + \delta_d dev(s) \mathrm{MRF}(s). \tag{25}$$

When the reference current is set to 15 A (rated current), it can be seen from Fig. 13(a) that the eight-sampled filter capacitor voltage without antialiasing filters contains the switching harmonics around 4, 8, 12, and 16 kHz. After using the MRF, all the sampled switching harmonics are removed [see Fig. 13(b)], which validates the effectiveness of MRF on noise suppression. The performance of MRF on the sampled converter-side current can be seen in [19] and [24], which is not further discussed in

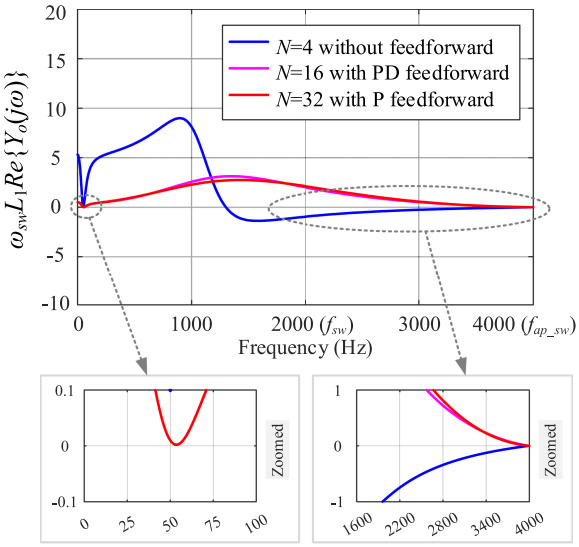

Fig. 19. Real part of output admittance for 4-sampling control, 16-sampling control with PD feedforward, and 32-sampling control with proportional feedforward.

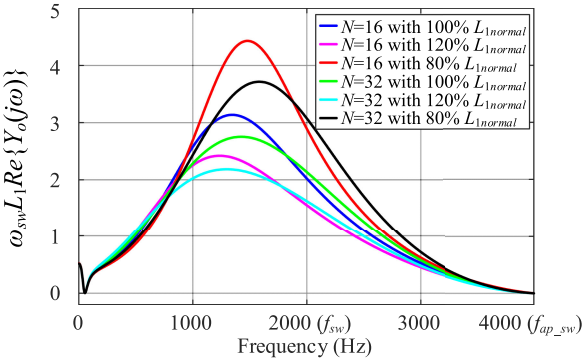

Fig. 20. Robustness analysis of the proposed method against converter-side inductance variation ($N = 16$ with PD feedforward or $N = 32$ with P feedforward).

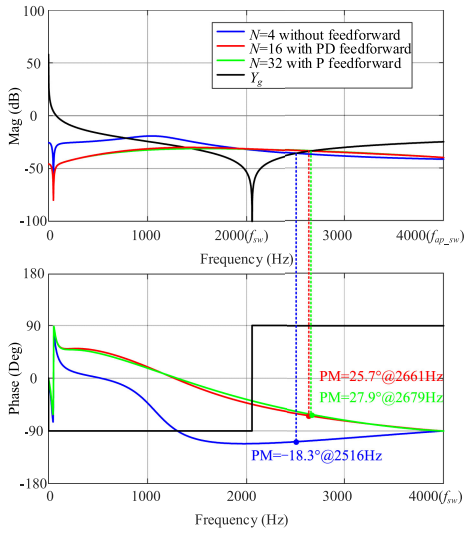

Fig. 21. Output admittance for a multisampled single-phase HB converter with and without the filter capacitor voltage feedforward.

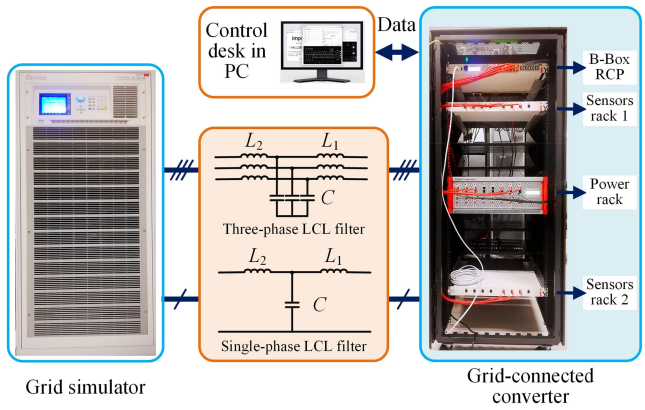

Fig. 22. Down-scaled single/three-phase grid-connected converter.

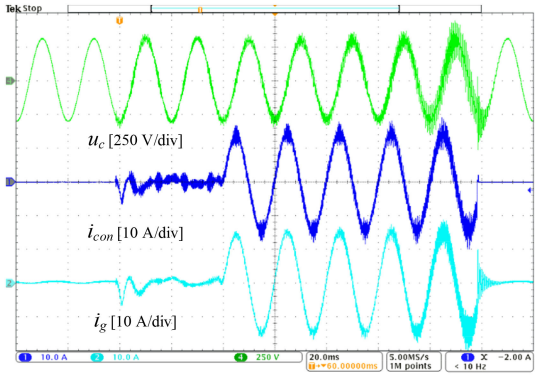

(a)

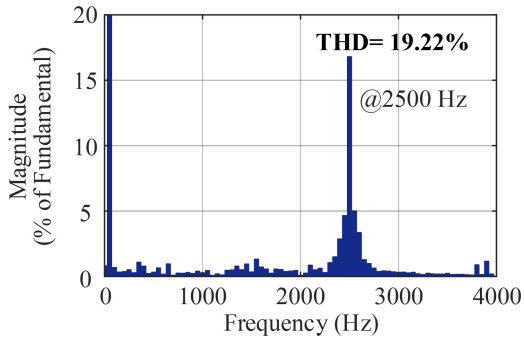

(b)

Fig. 23. Experimental results for a three-phase converter using $N = 8$ without feedforward. (a) Converter-side current and grid-side current. (b) Grid-side current harmonic spectrum.

this article. The average current and voltage can also be acquired using 16 samplings with MRF, and the attenuation r should be higher (see Table I). Based on Fig. 12, the converter output admittance using the feedforward scheme is

$$Y_o(s) = \frac{1 - e^{-sT_d}\delta_p \mathrm{MRF}(s) - e^{-sT_d}\delta_d dev(s)\mathrm{MRF}(s)}{sL_1 + e^{-sT_d}G_i(s)\mathrm{MRF}(s)}. \tag{26}$$

TABLE III
COMPARISON AMONG VARIOUS MULTISAMPLED CONTROL METHODS FOR SINGLE/THREE-PHASE CONVERTERS

Index \ Control methods	Three-phase converters			Single-phase HB converters			Single-phase CHB converters		
	N=8 without feedforward [27]	N=8 with PD feedforward	N=16 with P feedforward	N=4 without feedforward [28]	N=16 with PD feedforward	N=32 with P feedforward	N=4M without feedforward [29]	N=16M with PD feedforward	N=32M with PD feedforward
anti-aliasing filter	Yes	Yes	Yes	No	Yes	Yes	No	Yes	Yes
Loop delay	$(\frac{1.5}{8}+\frac{1}{4})T_{sw}$	$(\frac{1.5}{8}+\frac{1}{4})T_{sw}$	$(\frac{1.5}{16}+\frac{1}{4})T_{sw}$	$\frac{1.5}{4}T_{sw}$ ⇕ $\frac{1.5}{2}T_{ap\_sw}$	$(\frac{1.5}{16}+\frac{1}{8})T_{sw}$ ⇕ $(\frac{1.5}{8}+\frac{1}{4})T_{ap\_sw}$	$(\frac{1.5}{32}+\frac{1}{8})T_{sw}$ ⇕ $(\frac{1.5}{16}+\frac{1}{4})T_{ap\_sw}$	$\frac{1.5}{4M}T_{sw}$ ⇕ $\frac{1.5}{2}T_{ap\_sw}$	$(\frac{1.5}{16M}+\frac{1}{8M})T_{sw}$ ⇕ $(\frac{1.5}{8}+\frac{1}{4})T_{ap\_sw}$	$(\frac{1.5}{32M}+\frac{1}{8M})T_{sw}$ ⇕ $(\frac{1.5}{16}+\frac{1}{4})T_{ap\_sw}$
Dissipative region	$(0,\frac{4}{7}f_{sw})$	$(0, f_{sw})$	$(0, f_{sw})$	$(0,\frac{2}{3}f_{sw})$ ⇕ $(0,\frac{1}{3}f_{ap\_sw})$	$(0, 2f_{sw})$ ⇕ $(0, f_{ap\_sw})$	$(0, 2f_{sw})$ ⇕ $(0, f_{ap\_sw})$	$(0,\frac{2}{3}Mf_{sw})$ ⇕ $(0,\frac{1}{3}f_{ap\_sw})$	$(0, 2Mf_{sw})$ ⇕ $(0, f_{ap\_sw})$	$(0, 2Mf_{sw})$ ⇕ $(0, f_{ap\_sw})$

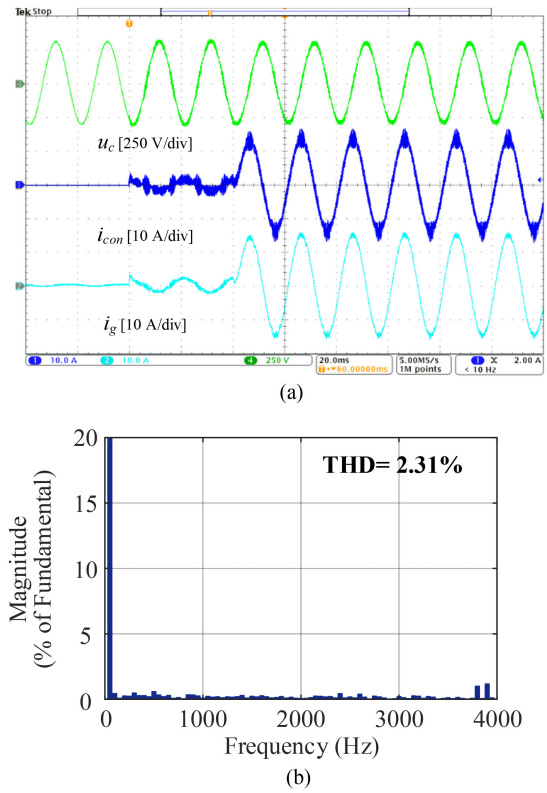

Fig. 24. Experimental results for a three-phase converter using $N = 8$ with PD feedforward. (a) Converter-side current and grid-side current. (b) Grid-side current harmonic spectrum.

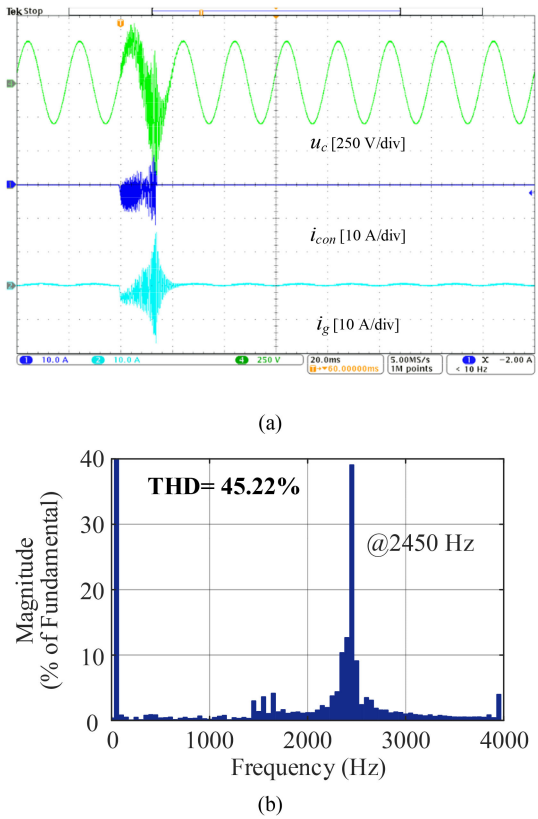

Fig. 25. Experimental results for a single-phase HB converter using $N = 4$ without feedforward. (a) Converter-side current and grid-side current. (b) Grid-side current harmonic spectrum.

It can be seen from Fig. 14 that $N = 8$ with P feedforward cannot achieve dissipation around the switching frequency, and $N = 8$ with PD feedforward can achieve dissipation below the switching frequency. That is because the delay compensator in (12) cannot make the loop delay small enough. If the sampling rate is further increased to 16, only using P feedforward can achieve dissipation. Moreover, the stability around the critical frequency is enhanced compared with $N = 8$ with D feedforward. It is known from (26) that the output admittance is related to the converter-side inductance, which might have a ±20% deviation from its nominal value. Fig. 15 shows a comparison of $\mathrm{Re}\{Y_o(j\omega)\}$ with the proposed method by considering ±20% variations of L_1. It can be seen that the dissipation can still be achieved and the proposed method performs robustly against filter inductance variations.

In terms of parameter design, K_p can be deduced based on a given PM or bandwidth. When using eight samplings, the D feedforward coefficient δ_d is first deduced based on (23). Then, the P feedforward coefficient δ_p is set to 0.85–0.9, and tune K_r until the nondissipative region in the low-frequency range is removed. It is worth noting that K_r can be set to a low value since the proportional feedforward is against with R controller

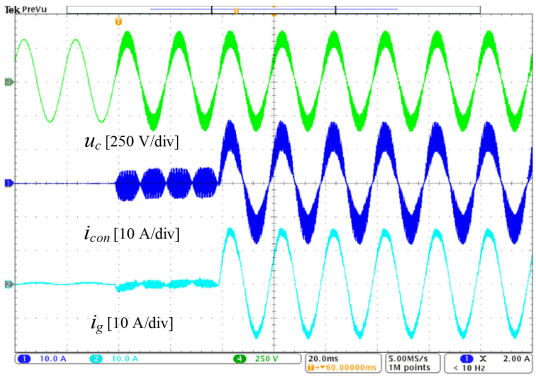

(a)

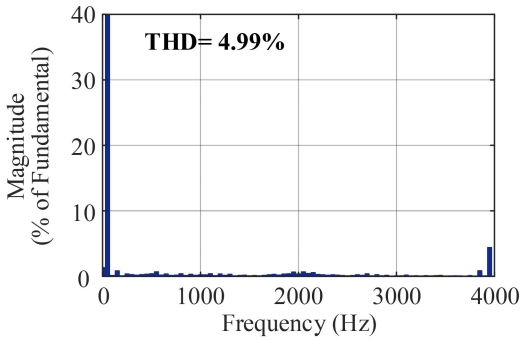

(b)

Fig. 26. Experimental results for a single-phase HB converter using $N = 16$ with PD feedforward. (a) Converter-side current and grid-side current. (b) Grid-side current harmonic spectrum.

in terms of the low-frequency dissipation [27]. Furthermore, K_r can also be set to zero with unity feedforward, but there will be an acceptable steady-state control error. When using 16 samplings, only the P feedforward coefficient δ_p and K_r need to be tuned.

Considering the admittance-based stability analysis, the filter capacitance and grid-side inductance can be regarded as the grid admittance, i.e., $Y_g(s) = sC+1/sL_2$. As shown in Fig. 16, the grid admittance intersects the converter output admittance in its negative-real-part region for $N = 8$ without feedforward, which leads to a $-4.6°$ PM. Hence, the system will be unstable. Nevertheless, the system can still be stabilized using the proposed method $N = 8$ with PD feedforward or $N = 16$ with P feedforward, and the PM for both proposed methods is similar.

C. Multisampled Control of Single-Phase Converters

As previously discussed in Section II-C, four-sampling control of a single-phase H-bridge converter can be regarded as a DS control seen from the apparent switching frequency f_{ap_sw}, i.e., the Nyquist frequency. To extend the dissipative region to f_{ap_sw}, the proposed method in the three-phase system can be extended by doubling the sampling rate. Specifically, the sampling frequency is set to $8f_{ap\_sw}$, i.e., $16f_{sw}$. Then, the MRF in (12) is used to remove the switching harmonics in the sampled voltage and current, where the sampling rate N is still set to eight and r is set to 0.6. When the sampling frequency is set to $16f_{ap\_sw}$, i.e., $32f_{sw}$, r is set to 0.8. More generally, for the CHB converter with M cells, the sampling frequency can be set to $8f_{ap\_sw}$ or $16f_{ap\_sw}$, i.e., $16Mf_{sw}$ or $32Mf_{sw}$. Fig. 17(a) shows the four-sampled converter-side current, and no switching harmonics are introduced as only the average value is sampled. When the sampling rate is 16, the switching harmonics around 4, 8, and 12 kHz are introduced, as shown in Fig. 17(b).

After using the MRF, most of the sampled switching harmonics are removed [see Fig. 17(c)]. Similarly, the filter capacitor average voltage cannot be acquired using 4 samplings and 16 samplings, as shown in Fig. 18(a) and (b). That is because the sampled value at the intersection points between the interleaved carriers is equal to the dc-link voltage, and the switching harmonics are introduced. When using 16 samplings with MRF, the switching harmonics are removed, as shown in Fig. 18(c). The average current and voltage can also be acquired under 32 samplings with MRF.

It can be seen from Fig. 19 that $N = 4$ without feedforward has a large nondissipative region as the four-sampling control is a kind of DS control based on the apparent switching frequency. On the other hand, the dissipative region is lifted to the apparent switching frequency when using $N = 16$ with PD feedforward. Similarly, $N = 32$ with P feedforward can also optimize the dissipative region to the apparent switching frequency. Considering $\pm 20\%$ deviation of the converter-side inductance, as shown in Fig. 20, the dissipation below the apparent switching frequency can still be achieved with the proposed method. It can be seen from Fig. 21 that the PM for the four-sampling control is negative, which leads to the system being unstable. Nevertheless, the system can still be stabilized using the proposed method $N = 16$ with PD feedforward or $N = 32$ with P feedforward, and the PM for both proposed methods is similar.

D. Summary

To further illustrate the similarities and the difference between the three-phase system and the single-phase system when using the proposed method, a comparison is given in Table III where with/without using an antialiasing filter, the loop delay, and the dissipative region are considered.

If only increasing the sampling rate without any damping terms, the nondissipative region always exists due to the delay ($0.25T_{sw}$) from the antialiasing filter. When using $N = 8$ with PD feedforward or $N = 16$ with P feedforward, the dissipative region can be optimized to the switching frequency. When using $N = 4$ without feedforward for a single-phase HB converter, the dissipative region is the same as the DS control based on the apparent switching frequency, which can also explain why the antialiasing filter is not required. Then, the sampling rate can be doubled, i.e., $N = 16$ with PD feedforward ($8f_{ap\_sw}$) or $N = 32$ with P feedforward ($16f_{ap\_sw}$). Furthermore, for a single-phase CHB converter with M cells, based on the apparent switching frequency, the damping method should be $N = 16M$ with PD feedforward ($8f_{ap\_sw}$) or $N = 32M$ with P feedforward ($16f_{ap\_sw}$). However, a high-performance digital processor with fast computation ability is required.

IV. Experimental Results

To further verify the theoretical analysis, experiments are carried out on a down-scaled single-phase and three-phase grid-connected converter with an *LCL* filter, as shown in Fig. 22. The grid is emulated with a chroma grid simulator model 61845. The applied half-bridge module and the control platform are a PEB-8024 module and a B-BOX RCP control platform from Imperix, respectively. The used current sensor is LEM CKSR 50-P with a bandwidth of 300 kHz. The related parameters of the single/three-phase grid-connected converter are presented in Tables I and II, respectively.

A. Three-Phase Converter

The experimental result using $N = 8$ without feedforward for the down-scaled three-phase converter is shown in Fig. 23(a). The converter starts at 40 ms, and the reference current is set to zero to suppress the inrush current during startup. Then, the reference current steps up to 15 A (rated current), and the system becomes unstable and the protection is triggered, which is consistent with the theoretical analysis in Fig. 16. In addition, it can be seen from Fig. 23(b) that the resonance frequency is 2500 Hz, which is close to the intersection frequency of 2601 Hz in Fig. 16, and the frequency drift is due to the parasitic resistor in series with the filter inductor. When using $N = 8$ with PD feedforward, the system stability is secured as well as the startup transients are suppressed, as shown in Fig. 24. The result using $N = 16$ with P feedforward is similar to the result in Fig. 24, which is not presented in this section.

B. Single-Phase HB Converter

The experimental result using $N = 4$ without feedforward for the down-scaled single-phase HB converter is shown in Fig. 25(a). Similarly, the system becomes unstable and the protection is triggered, which is consistent with the theoretical analysis in Fig. 21. In addition, it can be seen from Fig. 25(b) that the resonance frequency is 2450 Hz, which is close to the intersection frequency of 2516 Hz in Fig. 21. When using $N = 16$ with PD feedforward, the system stability is secured as well as the startup transients are suppressed, as shown in Fig. 26. The result using the $N = 32$ with P feedforward is similar to the result in Fig. 26, which is not presented in this section.

V. Conclusion

This article first investigates the dissipative region of single-loop multisampled control with converter-side current feedback. Due to the phase lag from the antialiasing filter in the feedback path, there is always a nondissipative region that threatens the stable operation. To overcome this bottleneck, a filter capacitor voltage feedforward scheme is proposed in this article. For the three-phase converter, eight samplings with PD feedforward or 16 samplings with proportional feedforward can achieve the dissipation in the whole frequency range. In addition, the stability around the critical frequency is enhanced compared with only using the derivative feedforward.

On the other hand, for the single-phase H-bridge converter, the apparent switching frequency (i.e., Nyquist frequency) is twice larger than the preset switching frequency and the four-sampling control is equivalent to a DS control. Then, the proposed method in the three-phase system is extended by doubling the sampling rate. Specifically, 16 samplings ($8f_{ap\_sw}$) with PD feedforward or 32 samplings ($16f_{ap\_sw}$) with proportional feedforward can lift the dissipative region to the apparent switching frequency. Furthermore, the proposed method can also be applied in the single-phase CHB converter. Finally, the experimental results validate the effectiveness of the proposed method.

References

[1] F. Blaabjerg, Y. Yang, D. Yang, and X. Wang, "Distributed power-generation systems and protection," *Proc. IEEE*, vol. 105, no. 7, pp. 1311–1331, Jul. 2017.

[2] X. Wang and F. Blaabjerg, "Harmonic stability in power electronic-based power systems: Concept, modeling, and analysis," *IEEE Trans. Smart Grid*, vol. 10, no. 3, pp. 2858–2870, May 2019.

[3] W. Wu, Y. Liu, Y. He, H. S.-H. Chung, M. Liserre, and F. Blaabjerg, "Damping methods for resonances caused by LCL-filter-based current-controlled grid-tied power inverters: An overview," *IEEE Trans. Ind. Electron.*, vol. 64, no. 9, pp. 7402–7413, Sep. 2017.

[4] M. Cespedes and J. Sun, "Impedance modeling and analysis of grid-connected voltage-source converters," *IEEE Trans. Power Electron.*, vol. 29, no. 3, pp. 1254–1261, Mar. 2014.

[5] L. Harnefors, X. Wang, A. G. Yepes, and F. Blaabjerg, "Passivity-based stability assessment of grid-connected VSCs—An overview," *IEEE J. Emerg. Sel. Topics Power Electron.*, vol. 4, no. 1, pp. 116–125, Mar. 2016.

[6] M. Aeberhard, M. Meyer, and C. Courtois, "The new standard EN 50388-2: Part 2—Stability and harmonics," *Elektrische Bahnen*, vol. 12, no. 1, pp. 28–35, 2014.

[7] L. Harnefors, A. G. Yepes, A. Vidal, and J. Doval-Gandoy, "Passivity-based controller design of grid-connected VSCs for prevention of electrical resonance instability," *IEEE Trans. Ind. Electron.*, vol. 62, no. 2, pp. 702–710, Feb. 2015.

[8] C. Xie, K. Li, J. Zou, and J. M. Guerrero, "Passivity-based stabilization of LCL-type grid-connected inverters via a general admittance model," *IEEE Trans. Power Electron.*, vol. 35, no. 6, pp. 6636–6648, Jun. 2020.

[9] D. Pan, X. Ruan, and X. Wang, "Direct realization of digital differentiators in discrete domain for active damping of LCL-type grid-connected inverter," *IEEE Trans. Power Electron.*, vol. 33, no. 10, pp. 8461–8473, Oct. 2018.

[10] Z. Xin, P. C. Loh, X. Wang, F. Blaabjerg, and Y. Tang, "Highly accurate derivatives for LCL-filtered grid converter with capacitor voltage active damping," *IEEE Trans. Power Electron.*, vol. 31, no. 5, pp. 3612–3625, May 2016.

[11] X. Wang, F. Blaabjerg, and P. C. Loh, "Passivity-based stability analysis and damping injection for multiparalleled VSCs with LCL filters," *IEEE Trans. Power Electron.*, vol. 32, no. 11, pp. 8922–8935, Nov. 2017.

[12] A. Akhavan, J. C. Vasquez, and J. M. Guerrero, "A simple method for passivity enhancement of current controlled grid-connected inverters," *IEEE Trans. Power Electron.*, vol. 35, no. 8, pp. 7735–7741, Aug. 2020.

[13] M. A. Awal, W. Yu, and I. Husain, "Passivity-based predictive-resonant current control for resonance damping in LCL-equipped VSCs," *IEEE Trans. Ind. Appl.*, vol. 56, no. 2, pp. 1702–1713, Mar./Apr. 2020.

[14] H. Wu and X. Wang, "Virtual-flux-based passivation of current control for grid-connected VSCs," *IEEE Trans. Power Electron.*, vol. 35, no. 12, pp. 12673–12677, Dec. 2020.

[15] S. Zhou, X. Zou, D. Zhu, L. Tong, and Y. Kang, "Improved capacitor voltage feedforward for three-phase LCL-type grid-connected converter to suppress start-up inrush current," *Energies*, vol. 10, no. 5, May 2017, Art. no. 713.

[16] X. Zhang, P. Chen, C. Yu, F. Li, H. T. Do, and R. Cao, "Study of a current control strategy based on multisampling for high-power grid-connected inverters with an LCL filter," *IEEE Trans. Power Electron.*, vol. 32, no. 7, pp. 5023–5034, Jul. 2017.

[17] L. Corradini, W. Stefanutti, and P. Mattavelli, "Analysis of multisampled current control for active filters," *IEEE Trans. Ind. Appl.*, vol. 44, no. 6, pp. 1785–1794, Nov./Dec. 2008.

[18] S. He, D. Zhou, X. Wang, Z. Zhao, and F. Blaabjerg, "A review of multisampling techniques in power electronics applications," *IEEE Trans. Power Electron.*, vol. 37, no. 9, pp. 10514–10533, Sep. 2022.
[19] S. He, D. Zhou, X. Wang, and F. Blaabjerg, "Aliasing suppression of multisampled current-controlled LCL-filtered inverters," *IEEE J. Emerg. Sel. Topics Power Electron.*, vol. 10, no. 2, pp. 2411–2423, Apr. 2022.
[20] H. Fujita, "A single-phase active filter using an H-bridge PWM converter with a sampling frequency quadruple of the switching frequency," *IEEE Trans. Power Electron.*, vol. 24, no. 4, pp. 934–941, Apr. 2009.
[21] J. Ma, X. Wang, F. Blaabjerg, W. Song, S. Wang, and T. Liu, "Multisampling method for single-phase grid-connected cascaded H-bridge inverters," *IEEE Trans. Ind. Electron.*, vol. 67, no. 10, pp. 8322–8334, Oct. 2020.
[22] D. Zhou and F. Blaabjerg, "Bandwidth oriented proportional-integral controller design for back-to-back power converters in DFIG wind turbine system," *IET Renewable Power Gener.*, vol. 11, no. 7, pp. 941–951, Jun. 2017.
[23] J. Ma, X. Wang, F. Blaabjerg, L. Harnefors, and W. Song, "Accuracy analysis of the zero-order hold model for digital pulse width modulation," *IEEE Trans. Power Electron.*, vol. 33, no. 12, pp. 10826–10834, Dec. 2018.
[24] S. He, D. Zhou, X. Wang, and F. Blaabjerg, "Line voltage sensorless control of grid-connected inverters using multisampling," *IEEE Trans. Power Electron.*, vol. 37, no. 4, pp. 4792–4803, Apr. 2022.
[25] S. Golestan, J. M. Guerrero, and A. M. Abusorrah, "MAF-PLL with phase-lead compensator," *IEEE Trans. Ind. Electron.*, vol. 62, no. 6, pp. 3691–3695, Jun. 2015.
[26] L. Harnefors, R. Finger, X. Wang, H. Bai, and F. Blaabjerg, "VSC input-admittance modeling and analysis above the Nyquist frequency for passivity-based stability assessment," *IEEE Trans. Ind. Electron.*, vol. 64, no. 8, pp. 6362–6370, Aug. 2017.
[27] L. Harnefors, L. Zhang, and M. Bongiorno, "Frequency-domain passivity-based current controller design," *IET Power Electron.*, vol. 1, no. 4, pp. 455–465, Jan. 2009.

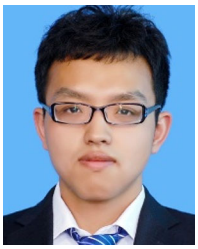

Shan He (Member, IEEE) received the B.S. degree from Northeast Electric Power University, Jilin, China, in 2015, and the M.S. degree from Zhejiang University, Hangzhou, China, in 2018, both in electrical engineering. He is currently working toward the Ph.D. degree in power electronics with Aalborg University, Aalborg, Denmark.

He was a Visiting Researcher with RWTH Aachen University, Aachen, Germany, from October 2021 to December 2021. His current research interests include modeling and control of grid-connected converters.

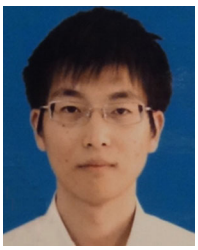

Dao Zhou (Senior Member, IEEE) received the B.S. degree from Beijing Jiaotong University, Beijing, China, in 2007, the M.S. degree from Zhejiang University, Hangzhou, China, in 2010, and the Ph.D. degree from Aalborg University, Aalborg, Denmark, in 2014, all in electrical engineering.

Since 2014, he has been with the Department of Energy Technology, Aalborg University, where he is currently an Assistant Professor. His research interests include modeling, control, and reliability of power electronics in renewable energy application.

Dr. Zhou was a recipient of the Renewable and Sustainable Energy Conversion Systems of the IEEE Industry Applications Society First Prize Paper Award in 2015 and Best Session Paper at Annual Conference of the IEEE Industrial Electronics Society (IECON) in Austria in 2013.

Xiongfei Wang (Senior Member, IEEE) received the B.S. degree in electrical engineering from Yanshan University, Qinhuangdao, China, in 2006, the M.S. degree in electrical engineering from the Harbin Institute of Technology, Harbin, China, in 2008, and the Ph.D. degree in energy technology from Aalborg University, Aalborg, Denmark, in 2013.

Since 2009, he has been with the Department of Energy, Aalborg University (AAU Energy), where he became an Assistant Professor in 2014, an Associate Professor in 2016, and a Professor and Leader of Electronic Power Grid (eGRID) Research Group in 2018. He has also been a part-time Professor with the KTH Royal Institute of Technology, Stockholm, Sweden, since 2020. His current research interests include modeling and control of power electronic converters and systems, stability and power quality of power-electronics-dominated power systems, and high-power converters.

Dr. Wang serves as a Co-Editor-in-Chief for IEEE TRANSACTIONS ON POWER ELECTRONICS and an Associate Editor for IEEE JOURNAL OF EMERGING AND SELECTED TOPICS IN POWER ELECTRONICS (JESTPE). He was a recipient of nine prize paper awards in the IEEE Transactions and Conferences, the 2016 AAU Talent for Future Research Leaders, the 2018 Richard M. Bass Outstanding Young Power Electronics Engineer Award, the 2019 IEEE PELS Sustainable Energy Systems Technical Achievement Award, the 2020 IEEE PES Prize Paper Award, the 2020 JESTPE Star Associate Editor Award, the 2022 Isao Takahashi Power Electronics Award, and the Highly Cited Researcher in the Web of Science in 2019.

Frede Blaabjerg (Fellow, IEEE) received the Ph.D. degree in electrical engineering from Aalborg University, Aalborg, Denmark, in 1995.

He was with ABB-Scandia, Randers, Denmark, from 1987 to 1988. He became an Assistant Professor in 1992, an Associate Professor in 1996, and a Full Professor of Power Electronics and Drives, in 1998. In 2017, he became a Villum Investigator. His current research interests include power electronics and its applications, such as in wind turbines, photovoltaic systems, reliability, harmonics, and adjustable speed drives. He has authored or coauthored more than 600 journal papers in the fields of power electronics and its applications. He is the co-author of four monographs and editor of ten books in power electronics and its applications.

Dr. Blaabjerg was a recipient of 32 IEEE prize paper awards, the IEEE PELS Distinguished Service Award in 2009, the EPE-PEMC Council Award in 2010, the IEEE William E. Newell Power Electronics Award 2014, the Villum Kann Rasmussen Research Award 2014, the Global Energy Prize in 2019, and the 2020 IEEE Edison Medal. He was the Editor-in-Chief for IEEE TRANSACTIONS ON POWER ELECTRONICS from 2006 to 2012. He was a Distinguished Lecturer for the IEEE Power Electronics Society from 2005 to 2007 and for the IEEE Industry Applications Society from 2010 to 2011 as well as 2017–2018. From 2019 to 2020, he was the President of IEEE Power Electronics Society. He is the Vice-President of the Danish Academy of Technical Sciences too. He is nominated in 2014–2019 by Thomson Reuters to be between the most 250 cited researchers in Engineering in the world.